

RESEARCH ARTICLE | NOVEMBER 05 2024

Ultra-low-energy defibrillation through adjoint optimization



Alejandro Garzón ; Roman O. Grigoriev



Chaos 34, 113110 (2024)

<https://doi.org/10.1063/5.0222247>



Articles You May Be Interested In

Control of electrical turbulence by periodic excitation of cardiac tissue

Chaos (November 2017)

The role of conductivity discontinuities in design of cardiac defibrillation

Chaos (January 2018)

Taming cardiac arrhythmias: Terminating spiral wave chaos by adaptive deceleration pacing

Chaos (December 2022)

Chaos

Special Topics Open
for Submissions

[Learn More](#)

Ultra-low-energy defibrillation through adjoint optimization

Cite as: Chaos 34, 113110 (2024); doi: 10.1063/5.0222247

Submitted: 6 June 2024 · Accepted: 24 September 2024 ·

Published Online: 5 November 2024



View Online



Export Citation



CrossMark

Alejandro Garzón^{1,a)}  and Roman O. Grigoriev² 

AFFILIATIONS

¹Department of Mathematics, Universidad Sergio Arboleda, Bogotá 110221, Colombia

²School of Physics, Georgia Institute of Technology, Atlanta, Georgia 30332-0430, USA

^{a)}Author to whom correspondence should be addressed: alejandro.garzon@usa.edu.co

ABSTRACT

This study investigates ultra-low-energy defibrillation protocols using a simple two-dimensional model of cardiac tissue. We find that, rather counter-intuitively, a single, properly timed, biphasic pulse can be more effective in defibrillating the tissue than low energy antitachycardia pacing (LEAP), which employs a sequence of such pulses, succeeding where the latter approach fails. Furthermore, we show that, with the help of adjoint optimization, it is possible to reduce the energy required for defibrillation even further, making it three orders of magnitude lower than that required by LEAP. Finally, we establish that this dramatic reduction is achieved through exploiting the sensitivity of the dynamics in vulnerable windows to promote the annihilation of pairs of nearby phase singularities.

Published under an exclusive license by AIP Publishing. <https://doi.org/10.1063/5.0222247>

Fibrillation is a type of cardiac arrhythmia that can be lethal unless quickly terminated. Existing protocols for terminating fibrillation employ a sequence of one or more electric pulses with a predefined temporal profile. These protocols require substantial energy and have many associated adverse effects, including intense pain and even heart tissue damage. The present study introduces an optimization approach that enables the reduction of the energy required for defibrillation by several orders of magnitude by allowing the applied electric field to have an arbitrary temporal profile.

I. INTRODUCTION

Fibrillation is a state of irregular and uncoordinated contraction of the cardiac muscle that can affect the ventricles or the atria, with serious physiological consequences. Ventricular fibrillation (VF), unless terminated, leads to sudden cardiac death, a major cause of mortality,¹ responsible for more than 370 000 deaths in the United States during 2019.² Atrial fibrillation (AF), while not fatal, is linked to an elevated risk of detrimental outcomes, like heart failure, dementia, and stroke.³ A 2010 study⁴ found 33.5×10^6 individuals affected by atrial fibrillation worldwide, with 5×10^6 new cases occurring that year, making this condition a global epidemic.

Fibrillation can be terminated by a high-energy electric shock that depolarizes a significant portion of the heart muscle, allowing restoration of the sinus rhythm. This is the standard approach used by both external defibrillators and implantable cardioverter defibrillators (ICDs), proven to extend the life of patients at high risk of lethal arrhythmias.⁵ However, these shocks tend to cause heart tissue damage^{6,7} and intense pain, possibly leading to anxiety, depression, and post-traumatic stress.^{8,9}

Therefore, a concerted effort has been devoted to developing low-energy defibrillation therapies. One of the oldest approaches is to use a time-periodic electric field with the frequency nearly matched to the natural frequency of the spiral waves to induce their resonant drift¹⁰ out of the tissue. As shown by Biktashev and Holden,¹¹ this can lead to an order of magnitude reduction in the energy, although this approach has a number of complications associated with inhomogeneity of the tissue and interaction of spiral waves with the tissue boundaries.¹²

An alternative approach, called Low Energy Antitachycardia Pacing (LEAP), uses a periodic sequence of lower energy pulses aiming to increase spatial synchronization. Several theoretical and experimental studies^{13–15} have shown that LEAP can eliminate fibrillation even when the energy of each pulse is an order of magnitude lower than that of the single-shock defibrillation protocol. An improvement to LEAP has been proposed by Lilienkamp *et al.*,¹⁶ who found in simulations that a gradual lengthening of

the time interval between consecutive pulses, in contrast to a fixed interval, can increase the probability of defibrillation. Similarly, a modulation of the interval between pulses, aimed at reducing the intercellular dispersion of the so-called isostable coordinates, was proposed by Wilson and Moehlis.¹⁷ A recent clinical investigation in humans¹⁸ verified successful termination of atrial fibrillation by means of a sequence of pulses of varying energy, some of those possibly below the pain threshold. DeTal *et al.*¹⁹ demonstrated a procedure to identify tissue regions where application of a single low-energy pulse by multiple electrodes can terminate reentrant waves.

These studies suggest that painless defibrillation via a sequence of low-energy pulses might become a reality in clinical practice, in the near future. However, even if this favorable scenario materializes, the quest for a further reduction of the energy of the defibrillating protocols should not stop, as pain is only one adverse effect. It is not unreasonable to suspect long-term tissue damage even from low-energy pulses considering that the termination of AF might be, for some patients, a frequent occurrence. For instance, the investigation of Gold *et al.*²⁰ on the efficacy of an ICD to stop AF found a mean rate of seven treated episodes of atrial tachyarrhythmias per patient-month. Moreover, these numerous treatments imply fast battery drainage, reducing the lifetime of an ICD and increasing mortality risks associated with its surgical replacement.²¹ In this regard, it is worth noting that, for some therapies based on sequences of low energy pulses, although the per-pulse energy is lower, compared to single shock therapy, the total energy is similar,¹⁵ so LEAP might not increase the lifetime of ICDs.

Given the potential advantages of a further reduction of the energy required for defibrillation, the question arises as to both how defibrillation protocols with an even lower energy can be identified and how much the energy can be reduced. Single-shock defibrillation offers little room for improvement, although some signal shape optimization has been attempted.^{22,23} LEAP offers more opportunities for optimization by varying the number of pulses, the inter-pulse time, and the single-pulse energy; searches in this low-dimensional parameter space have been attempted as well.¹⁴ This approach has the limitation of restricting the search to a narrow family of signals. While this family can be expanded somewhat by allowing the pulse strengths and inter-pulse intervals to vary independently,²⁴ this only allows a moderate reduction of the energy.

In the present work, we describe a systematic procedure for finding defibrillating signals with low energy in a two-dimensional model of cardiac tissue representing the atria. The search space is expanded to include continuous functions of time, representing an externally applied electric field, on a finite time interval. Our approach aims to minimize the total energy of the defibrillation protocol while simultaneously maximizing the success rate using adjoint optimization. A similar approach has been used previously in a much more restricted capacity to optimize the signal shape for single-shock defibrillation on a very brief temporal interval (4 ms).²³ In contrast, in this work, we consider signals over much longer time intervals comparable to the LEAP protocol, i.e., several characteristic periods of spiral wave revolution.

The paper is structured as follows. In Sec. II, the electrophysiological model, the optimization problem, and its solution through adjoint optimization are described. The results are presented in

Sec. III, which compares different defibrillation protocols. Conclusions and perspectives are offered in Sec. IV.

II. PROBLEM DESCRIPTION

To highlight the generality of our approach, it is discussed in terms of an electrophysiological model of cardiac tissue with n state variables that can describe atria (or ventricles) when defined in two (or three) spatial dimensions. Let $u_1(t, \mathbf{r})$ represent the transmembrane voltage and $u_2(t, \mathbf{r}), \dots, u_n(t, \mathbf{r})$ be the gating variables. Here, t denotes time and \mathbf{r} denotes the spatial position of cells in the domain Ω , which contains non-conducting patches representing anatomical heterogeneities, such as blood vessels. The dynamics are described by a system of coupled partial differential equations

$$\partial_t \mathbf{u} = \tilde{\mathbf{L}}\mathbf{u} + \tilde{\mathbf{F}}(\mathbf{u}), \quad (1)$$

where $\mathbf{u} = [u_1, u_2, \dots, u_n]^T$ is the state vector and $\tilde{\mathbf{L}}\mathbf{u} = [D_1 \nabla^2 u_1, D_2 \nabla^2 u_2, \dots, D_n \nabla^2 u_n]^T$ describes the electrical coupling between cells. A small diffusion coefficient $D_i \ll D_1$, $i = 2, \dots, n$, is assumed for the gating variables, in order for the model to possess smooth solutions. Finally, $\tilde{\mathbf{F}}(\mathbf{u})$ represents the local membrane dynamics (ionic model).

In the presence of an external electric field $\mathbf{E}(t, \mathbf{r})$, the scaled voltage u_1 satisfies the boundary condition²⁵

$$\mathbf{n} \cdot (\nabla u_1 - \mathbf{E}) = 0, \quad (2)$$

where \mathbf{n} is the unit vector normal to the domain boundary $\Gamma = \partial\Omega$, which includes the boundaries of the heterogeneities. For the gating variables u_i , $i = 2, \dots, n$, no-flux boundary conditions are assumed

$$\mathbf{n} \cdot \nabla u_i = 0. \quad (3)$$

In the absence of an external electric field, the system has (i) a uniform equilibrium solution $\mathbf{u}(t, \mathbf{r}) = \mathbf{u}^*$, which describes the (stable) quiescent state corresponding to a total lack of electrical activity in the tissue and (ii) solutions describing persistent spiral wave chaos, which represents fibrillation. The goal of defibrillation is, therefore, to suppress chaotic dynamics in favor of the quiescent state by means of an appropriately chosen external electric field $\mathbf{E}(t, \mathbf{r})$.

For simplicity, we assume the applied electric field to be spatially uniform but varying in time. Choosing the x -axis pointing in the direction of the field, we have $\mathbf{E}(t, \mathbf{r}) = E(t)\hat{\mathbf{x}}$, where the hat denotes a unit vector. A time-dependent electric field $E(t)$ applied within a finite temporal window $0 < t < T$ leads to successful defibrillation if $\mathbf{u}(t, \mathbf{r})$ approaches the quiescent state \mathbf{u}^* within this finite window or soon after. Up to a dimensional prefactor, the total energy delivered to the tissue is given by

$$\mathcal{N} = \int_0^T [E(t)]^2 dt. \quad (4)$$

The quiescent state \mathbf{u}^* is spatially uniform, but it does not need to be reached by $t = T$. In fact, defibrillation can be achieved by simply eliminating spatial gradients (i.e., dispersion) of all the state variables by this time. Hence, an optimal defibrillating signal can be found by

minimizing the functional \mathcal{L}

$$\mathcal{L} = \frac{\alpha}{2}\mathcal{N} + \frac{1}{2}\mathcal{M}, \quad (5)$$

where

$$\mathcal{M} = \sum_{i=1}^n \gamma_i \mathcal{J}_i, \quad \mathcal{J}_i = \int_{\Omega} |\nabla u_i|_{t=T}^2 d\Omega, \quad (6)$$

and α and γ_i are positive parameters. The first term in (5) represents the total energy and the second term minimizes the gradients of the voltage and gating variables at the end of the interval. Parameters α and γ_i can be tuned to emphasize the relative importance of the gradients and the energy of the defibrillation signal. For instance, large values of γ_i 's will result in a faster but less energy-efficient defibrillation protocol while smaller values will result in a slower but more energy-efficient defibrillation protocol. Successful defibrillation would require the ratios γ_i/α to be sufficiently large.

For fixed model parameters, initial condition $\mathbf{u}_0(\mathbf{r})$, and the final time T , \mathcal{L} depends solely on $E(t)$. In other words, it is a functional defined over the set of all possible $E(t)$. To minimize \mathcal{L} , the gradient descent method will be used, which requires the calculation of the associated functional derivative,

$$\mathcal{G}(t) = \frac{\delta \mathcal{L}}{\delta E(t)}, \quad 0 \leq t \leq T. \quad (7)$$

The procedure used to evaluate this derivative is presented in Appendix A. Let us consider a continuous family of functions $E_s(t)$, where s is a continuous parameter, such that

$$\frac{dE_s(t)}{ds} = -\mathcal{G}(t)|_{E_s(t)}. \quad (8)$$

Then, $\mathcal{L}[E_s(t)]$ is a non-increasing function of s with the minima corresponding to a vanishing $\mathcal{G}(t)$. An optimal electric field minimizing \mathcal{L} can, therefore, be found by solving the differential Eq. (8) numerically, e.g., using finite differences, starting from an appropriate initial condition $E_0(t)$.

The simplest way to compute the functional derivative is using finite differences, as explained in Appendix A. For a numerical solution evaluated on a discrete temporal grid $t_l = l\Delta t$, $l = 0, 1, \dots, N$, where $\Delta t = T/N$ is the time step, the cost of evaluating $\mathcal{G}(t)$ scales as N^2 . This evaluation becomes prohibitively expensive for longer temporal intervals. We, therefore, employed an alternative method for calculating $\mathcal{G}(t)$ whose cost scales linearly with N . This approach, known as the adjoint method, is more clearly explained in terms of the spatial discretization of the model (1), as described next.

A. Spatial discretization

The spatial domain Ω was chosen as a square containing circular (non-conducting) heterogeneities with radii and locations selected randomly. The radii followed the power-law probability distribution,¹³ whereas the locations were distributed uniformly. Enough locations were selected to yield an average density of 16 heterogeneities per cm^2 . The solution $\mathbf{u}(t, \mathbf{r})$ of (1) was evaluated on a uniform square grid with 256 points on each side, with the grid points inside the heterogeneities excluded. This resulted in a computational grid with $m = 64\,071$ points. The grid spacing was chosen

to be $\Delta x = \Delta y = 0.035$ cm, which translates to a domain side length of 8.925 cm.

Let \mathbf{w} denote the discretization of $\mathbf{u}(t, \mathbf{r})$, where $\mathbf{w} = [u_{11}, \dots, u_{1m}, \dots, u_{n1}, \dots, u_{nm}]^T$, $u_{ij} \approx u_i(\mathbf{r}_j)$, and \mathbf{r}_j is the position of the j th grid point. Second-order finite differences were used to represent the Laplacian $\nabla^2 u_i$ and the derivatives in the boundary conditions (2) and (3). The dynamics of the tissue is then described by a system of coupled ODEs

$$\dot{\mathbf{w}} = L\mathbf{w} + F(\mathbf{w}) + E\mathbf{b}, \quad (9a)$$

$$\mathbf{w}(0) = \mathbf{w}_0, \quad (9b)$$

where L and F represent discretizations of \tilde{L} and \tilde{F} , respectively, and the term $E(t)\mathbf{b}$ represents the effect of the electric field. The cost function (5) can also be expressed in terms of \mathbf{w} ,

$$\mathcal{M} \approx [\mathbf{w}^T R \mathbf{w}]_{t=T}, \quad (10)$$

where R is a block-diagonal matrix. The details are given in Appendix B.

B. Adjoint method

We will follow the “adjoint looping” approach used previously in geophysics,²⁶ fluid dynamics,^{27,28} and plasma physics.²⁹ It involves the adjoint field $\lambda(t)$, which is a solution of the initial value problem,

$$-\dot{\lambda} = (L + J_F)^T \lambda, \quad (11a)$$

$$\lambda(T) = R\mathbf{w}(T), \quad (11b)$$

where $J_F = dF/d\mathbf{w}$ is the Jacobian of $F(\mathbf{w})$. The derivation is presented in Appendix C.

The adjoint method involves an iterative procedure entailing the following steps. First, the boundary value problem (9) is solved forward in time, which determines $\lambda(T)$. Next, $\lambda(t)$ is found by solving the initial value problem (11) backward in time. Note that solution of this problem requires evaluation of the Jacobian J_F at each time $0 \leq t \leq T$, which requires the entire solution $\mathbf{w}(t)$ to be stored. Next, the functional derivative of the cost function is evaluated as

$$\mathcal{G}(t) = \alpha E(t) + \mathbf{b}^T \lambda(t). \quad (12)$$

All variables are evaluated using $E(t) = E_s(t)$. Finally, the electric field is updated according to

$$E_{s+\Delta s}(t) = E_s(t) - \Delta s \mathcal{G}(t)|_{E_s(t)}, \quad (13)$$

with Δs sufficiently small to approximate the continuous solution of Eq. (8). The entire process is then repeated until convergence of $E(t)$ is achieved.

III. SPIRAL WAVE CHAOS AND DEFIBRILLATION PROTOCOLS

In this work, simulations were carried out for the three-variable Fenton–Karma model³⁰ of ionic dynamics. The parameters used are shown in Table I. To facilitate the computation of spatial derivatives of the gating variables and the Jacobian J_F , the Heaviside step

TABLE I. Parameters used in the Fenton–Karma model. All time scales are in units of milliseconds. The rest of the parameters are nondimensional.

Parameter	Value	Parameter	Value	Parameter	Value
u_c	0.13	τ_v^+	3.324	k	15
u_v	0.04	τ_0	8.2	τ_w^-	68
τ_d	0.388	τ_r	33.264	τ_w^+	400
τ_{v1}^-	7.6	τ_{si}	29.0		
τ_{v2}^-	8.8	u_c^{st}	0.54		

functions $\Theta(\chi)$ used in the model were replaced by their smoothed analogs,

$$\Theta_a(\chi) = \frac{1 + \tanh(\chi/a)}{2}, \quad (14)$$

with parameter $a = 0.01$ defining the width of the “step.” The diffusion coefficients were set to $D_1 = 10^{-3} \text{ cm}^2/\text{ms}$ and $D_2 = D_3 = 10^{-5} \text{ cm}^2/\text{ms}$. Solutions of Eqs. (9) and (11) were computed using fourth-order Runge–Kutta method with a time-step size $\Delta t = 0.1 \text{ ms}$. To speed up the computations, the integration function was implemented using CUDA (Nvidia Inc.) for execution on general-purpose graphics processing units. For ease of use, the CUDA code was then wrapped in MATLAB (Mathworks Inc.) mex-functions.

A pair of reentrant waves was generated using an S1–S2 protocol. First, the quiescent state $(u_1, u_2, u_3) = (0, 1, 1)$ was excited at a corner (S1 stimulus) by setting $u_1 = 1$ to produce a circular excitation wave. Note that the transmembrane voltage is given by $V = V_0 + (V_{fi} - V_0)u_1$, where $V_0 = -85 \text{ mV}$ is the reference voltage corresponding to the quiescent state and $V_{fi} = 15 \text{ mV}$.³⁰ A short time after the waveback had passed the center of the domain, a small patch of tissue was excited at the center (S2 stimulus). From the stimulated patch, a circular wave develops and produces a conduction block when meeting the back of the previous wave, generating a pair of spiral waves.

Figure 1(a) shows the voltage (u_1) about 1 s after the S2 stimulus. In the absence of an electric field $E(t)$, this initial condition gives rise to a state of persistent spiral wave chaos that lasts more than 20 s. For reference, the characteristic revolution time for a spiral wave is two orders of magnitude smaller, as shown below. Hence, in this system, spiral wave chaos represents either a sustained state (an attractor) or a long-lived transient (chaotic repeller). Figure 1 displays characteristic snapshots of the voltage field at different times with a corresponding movie provided as a multimedia file (available online). The state shown in Fig. 1(a) which features two phase singularities, was used as a representative initial condition \mathbf{u}_0 to compare the different defibrillation protocols discussed below. Other choices produced qualitatively similar results and hence are not discussed here. One exception is the state at $t = 10.77$ which features seven phase singularities and is considered briefly at the end of Sec. III C.

A. Defibrillation by sequences of pulses

Below we explore conventional biphasic single-pulse defibrillation protocol and LEAP to obtain a set of reference results. A key

parameter of LEAP is the typical period of the electrical activity during fibrillation, which corresponds to one revolution of a spiral wave. That period can be identified with the help of the power spectral density $W(f)$ (see Appendix D). A sample power spectrum for the solution with the initial condition depicted in Fig. 1(a) is shown in Fig. 2. The maximum of $W(f)$ at around $f = 4.7 \text{ Hz}$ corresponds to a typical period $P \approx 210 \text{ ms}$.

To examine single-pulse defibrillation, an asymmetric biphasic pulse was applied to the tissue,

$$E(t) = E^* g_p(t - t^*), \quad (15)$$

where E^* is the pulse strength, t^* is the pulse timing, and

$$g_p(t) = \Theta_a(t) - 2\Theta_a(t - 0.7p) + \Theta_a(t - p) \quad (16)$$

with Θ_a defined in Eq. (14), $a = 0.1 \text{ ms}$, and the pulse duration is $p = 10 \text{ ms}$. Pulses with smooth edges were used to allow the application of high-order integration methods for Eq. (9a). The pulse timing was changed from $t^* = 0 \text{ ms}$ up to $t^* = 200 \text{ ms}$ in steps of 20 ms, to target the different phases of the excitation dynamics. For simplicity, we consider fibrillation terminated when a state with transmembrane voltage $u_1 < 0.1$ in the entire tissue domain is reached (it is straightforward to reformulate this condition in terms of the spatial heterogeneity \mathcal{M}). An instance of successful defibrillation was declared if such a state was reached during an interval of time less than $5P = 1050 \text{ ms}$, measured from the end of the pulse. Table II shows our results for different pulse strengths E^* and the associated energies \mathcal{N} . Note how the likelihood of defibrillation decreases as the pulse strength E^* diminishes so that for $E^* = 0.5 \text{ V/cm}$ no defibrillation is observed for the values of t^* examined.

The likelihood of defibrillation can be increased using the LEAP protocol. This method employs a sequence of M pulses, with pulse separation usually chosen close to the typical period P of the fibrillatory electrical activity. For our investigation of LEAP, we used the external electric field

$$E(t) = E^* \sum_{m=0}^{M-1} g_p[t - (t^* + mP)], \quad (17)$$

where the pulses are biphasic [g_p is defined by Eq. (16)], have the same strength E^* , and are applied at times $t^*, t^* + P, \dots, t^* + (M-1)P$, with $P = 210 \text{ ms}$. A thorough statistical analysis of LEAP for a large ensemble of initial conditions has been conducted previously.³¹ Here, we focus on how the success of LEAP depends on parameters M , t^* , and E^* for a specific initial condition.

Figure 3 shows the termination time (measured from the end of the last pulse) for a pulse strength $E^* = 3 \text{ V/cm}$, different number of pulses M , and time t^* varied in steps of 1 ms. The dashed line marks the $5P$ threshold used to declare defibrillation. Note how the likelihood of defibrillation greatly increases with the number of pulses. In Ref. 15, synchronization of the excitation was identified as the mechanism for LEAP defibrillation. More exactly, it was found that each LEAP pulse increases the spatial homogeneity of the phase of the excitation wave across the tissue, thus raising the probability of defibrillation. The results shown in Fig. 3 are consistent with this mechanism. We also find that, even at this relatively high value of E^* , LEAP can fail for some choices of t^* . Moreover, additional

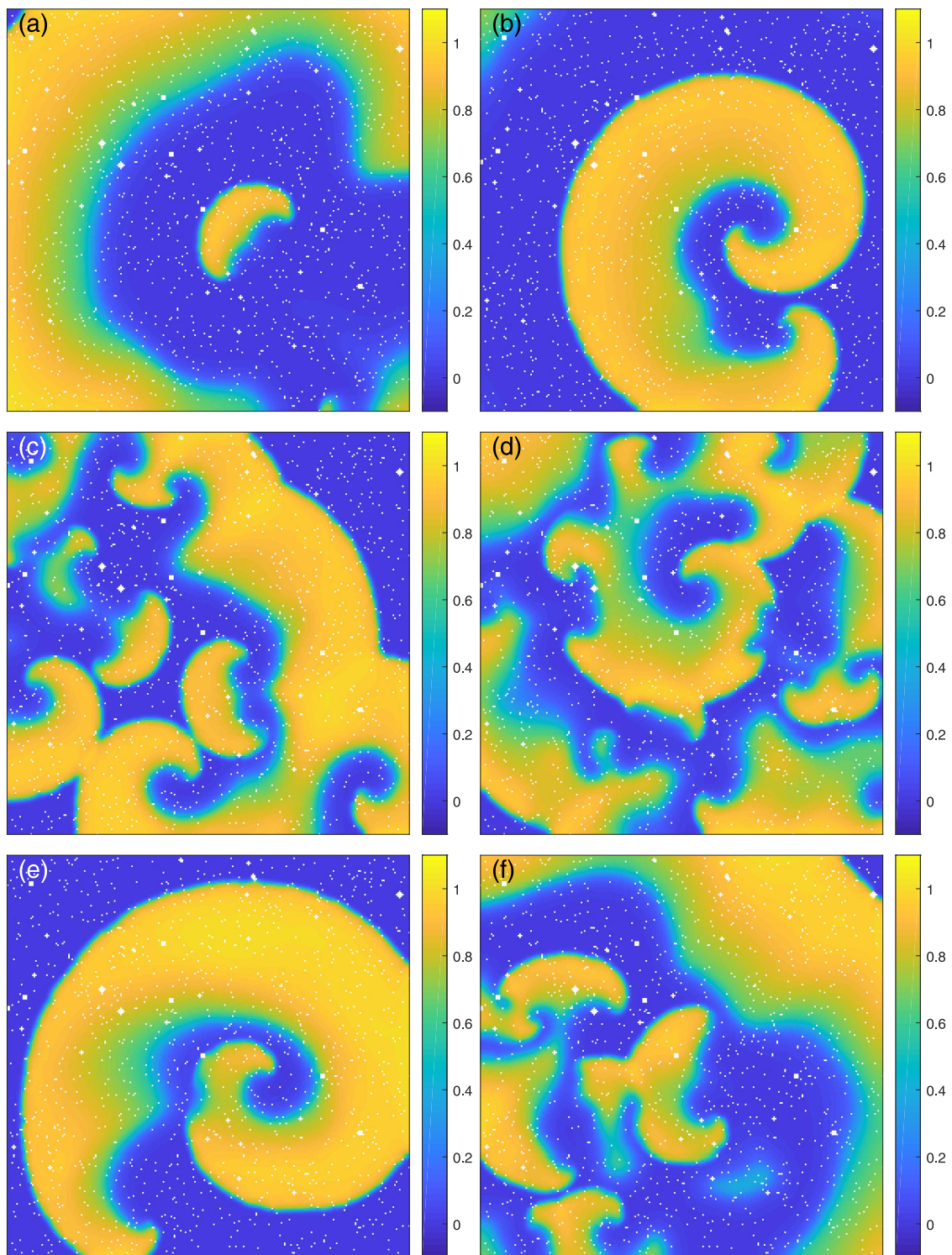


FIG. 1. Snapshots of the voltage field (u_1) describing a state of fibrillation at times (a) $t = 0$ ms, (b) $t = 290$ ms, (c) $t = 2.09$ s, (d) $t = 6.83$ s, (e) $t = 13.34$ s, and (f) $t = 20$ s. Nonconducting heterogeneities are shown in white. Multimedia available online.

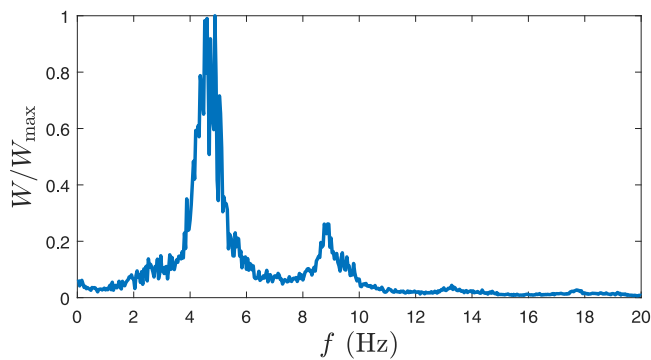


FIG. 2. Power spectrum of the electrical activity normalized by $W_{\max} = \max_f W(f)$.

pulses can have an adverse effect, with $M + 1$ pulses failing to defibrillate the tissue when M pulses would eventually succeed, as can be seen by comparing the results for $M = 4$ and $M = 5$. Nonetheless, the likelihood of successful termination of fibrillation is over 90% for this choice of E^* ; we can use the corresponding energy $\mathcal{N}_5 = 87.5 \text{ V}^2 \text{ ms/cm}^2$ as a benchmark to compare our results against.

LEAP becomes progressively more inefficient in inducing synchronization as the pulse strength is decreased. Figure 4 shows the termination time for $E^* = 1.5 \text{ V/cm}$ and the same combination of values of M and t^* as in Fig. 3. While the likelihood of defibrillation is again found to increase with M , it increases much more slowly, as comparison of Figs. 3 and 4 makes quite clear.

On the other hand, both Figs. 3 and 4 have an interesting common feature: for all values of E^* and M considered, one finds instances of successful defibrillation flanked on both sides by failures. Similarly, one finds failures flanked by successful outcomes. The same result would be found if the resolution of sampling in terms of t^* were decreased. This suggests that the measure, in terms of t^* , on which LEAP is successful is fractal. Indeed, a sequence of pulses can be thought of as setting up a particular initial condition \mathbf{u} that, for a fixed M , is a continuous function of E^* and t^* in the infinite-dimensional state space of the autonomous system (1). Fractal dependence on t^* suggests that the boundary between the two attractors, one representing continuing fibrillation (e.g., failed defibrillation) and the other representing the stable equilibrium

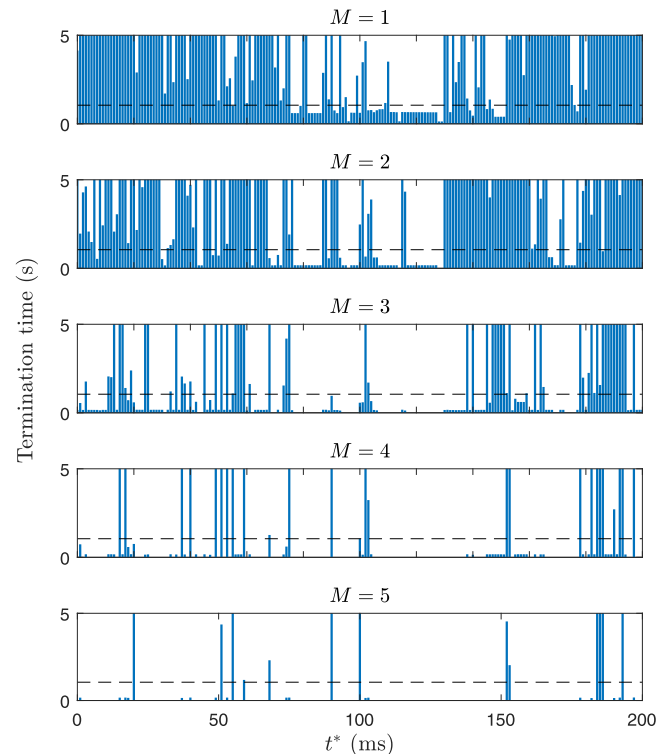


FIG. 3. Termination time (bar height) of electrical activity for LEAP signals defined by Eq. (17), with pulse strength $E^* = 3 \text{ V/cm}$, number of pulses M indicated above each panel, and timing t^* varied on steps of 1 ms. A bar that reaches the top edge of the axis box corresponds to a termination time above 5 s, not determined, possibly infinite. On each panel, the horizontal dashed line marks the threshold of 5P used to declare defibrillation.

(e.g., successful defibrillation) is fractal. This is analogous to what is found in transitional fluid turbulence,³² where the two attractors represent turbulent and laminar flow. It is important to note that the qualitative picture does not change even when chaotic dynamics represent a long-lived transient described by a chaotic repeller rather than a chaotic attractor.

To confirm the fractal structure of the basin boundary, we explored the dependence of the outcome on parameters for the

TABLE II. Defibrillation by a single pulse as defined by Eq. (15). Conventions: ■ (defibrillation), □ (no defibrillation).

E^* (V/cm)	\mathcal{N} ($\text{V}^2 \text{ ms/cm}^2$)	t^* (ms)										
		0	20	40	60	80	100	120	140	160	180	200
0.5	2.43	□	□	□	□	□	□	□	□	□	□	□
1	9.72	□	■	■	□	□	□	□	□	□	□	□
1.5	21.9	□	□	□	□	■	□	□	□	□	□	□
3	87.5	□	□	□	□	□	■	■	■	□	□	□
5	243	□	□	□	■	□	■	■	■	□	□	□
8	622	■	□	■	■	□	■	■	■	■	□	□

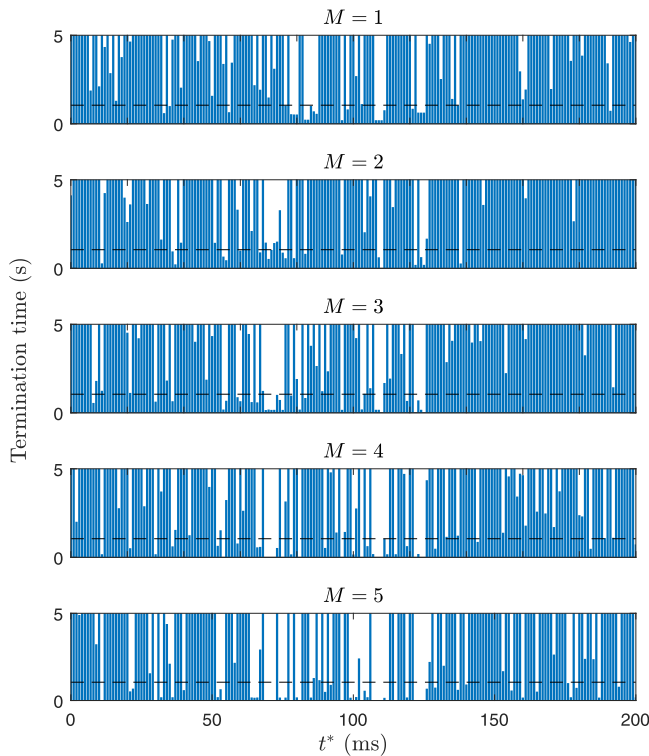


FIG. 4. Termination time of electrical activity for LEAP signals with pulse strength $E^* = 1.5$ V/cm, number of pulses M indicated above each panel, and timing t^* varied on steps of 1 ms. On each panel, the horizontal dashed line marks the threshold of $5P$ used to declare defibrillation.

single-pulse defibrillation protocol ($M = 1$). Specifically, we performed two sets of calculations by varying either the pulse strength or the pulse timing. In the first case, the pulse timing was fixed at $t^* = 20$ ms and the pulse strength E^* was varied in steps of 10^{-4} V/cm, around $E^* = 0.5$ V/cm. In the second case, the pulse strength was fixed at $E^* = 0.5$ V/cm (which corresponds to the energy of $\mathcal{N}_1 = 2.43$ V²ms/cm²) and the pulse timing t^* was varied in steps of 0.1 ms. As Fig. 5 illustrates, in both cases, we find the pattern noted previously, i.e., a sensitive, nonmonotonic, and non-smooth dependence of the defibrillation time on parameters, which is consistent with a fractal structure of the basin boundary. A similar sensitivity to the timing of the pulse has also been found by Steyer *et al.*³³

These results also illustrate that it is, in principle, possible to terminate fibrillation using a very simple low-energy protocol, i.e., a properly timed *single* biphasic pulse, with the energy which is one or two orders of magnitude smaller than that of a typical LEAP sequence. While the requirement to finely tune the parameters (here, E^* and t^*) makes this approach impractical, its success raises the fundamental question of whether the energy can be reduced even further by optimizing the temporal profile of the electric field $E(t)$. Hence, in Sec. III B, we use the adjoint method to construct such optimal profiles.

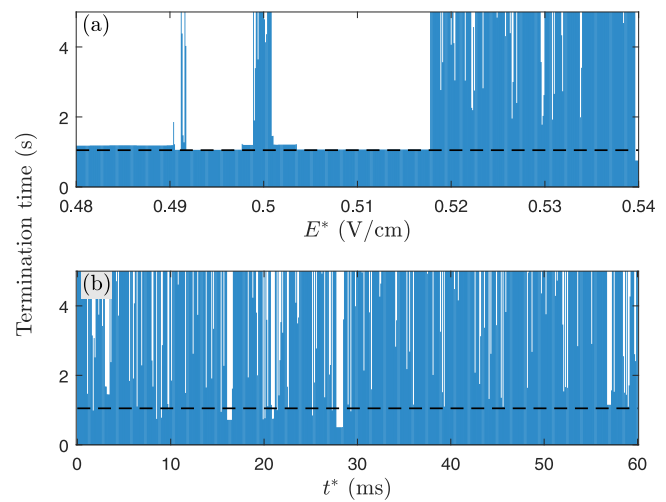


FIG. 5. Termination time of electrical activity for a single low-energy pulse. (a) Fixed time $t^* = 20$ ms and pulse strength E^* changed on steps of 10^{-4} V/cm. (b) Fixed $E^* = 0.5$ V/cm and pulse timing t^* varied on steps of $\Delta t = 0.1$ ms. On each panel, the horizontal dashed line marks the threshold of $5P$ used to declare defibrillation.

B. Optimal defibrillation protocols

The functional \mathcal{L} is defined over a space of functions $E(t)$ with finite support $t \in [0, T]$ and, for a given initial state \mathbf{u}_0 (or its discretization \mathbf{w}_0), it can have infinitely many local minima. The distance between these minima will generally decrease as T is increased, creating a rough “landscape” featuring both shallow and deep minima. Since we are mainly interested in the deep minima which correspond to small values of \mathcal{M} and \mathcal{N} , the choice of both T and the initial guess $E_0(t)$ for the gradient descent plays an important role. As we will see below, a poor choice of $E_0(t)$ may not allow finding solutions with particularly low energy \mathcal{N} , while poor choices of T may lead to extremely slow convergence.

Consider first an initial condition $E_0(t)$ that is close to a defibrillating signal with a relatively high energy. As we found previously, a single pulse with $(E^*, t^*) = (0.5$ V/cm, 20 ms) does not produce defibrillation, but it can become a defibrillating signal if small adjustments are applied to either E^* or t^* . Alternatively, the electric field $E_0(t)$ corresponding to such a single pulse can be modified slightly over a finite time interval by applying adjoint optimization. For instance, after a minimization over the interval $0 \leq t \leq T$, $T = 300$ ms, a defibrillating signal was found with energy $\mathcal{N} = 0.926$ V² ms/cm², which corresponds to 38% of the single-pulse energy \mathcal{N}_1 and 1% of the characteristic LEAP energy \mathcal{N}_5 . For reference, the following hyperparameters were used: $\Delta s = 10^{-5}$ (V/cm)², $\alpha = 50$ cm²/(V² ms), and $(\gamma_1, \gamma_2, \gamma_3) = (1, 0.2, 0.2)$.

During the minimization, both the spatial heterogeneity \mathcal{M} and the energy \mathcal{N} gradually decrease. The latter is shown in Fig. 6, with the color-coding describing the result (success/failure of defibrillation). While electric field profiles close to $E_0(t)$ fail to defibrillate the tissue, further minimization identifies electric field profiles

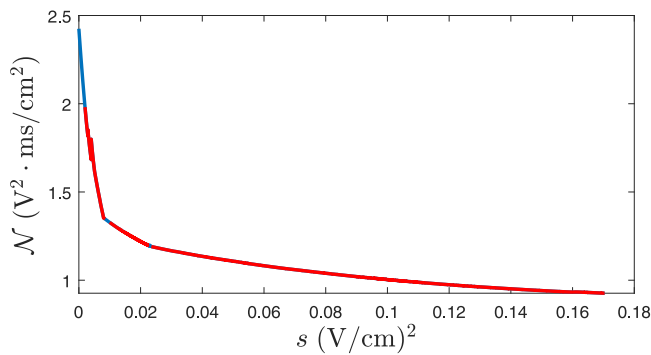


FIG. 6. The energy \mathcal{N} as a function of s for initial electric field $E_0(t)$ corresponding to the single pulse with $(E^*, t^*) = (0.5 \text{ V/cm}, 20 \text{ ms})$. The electric field was optimized over an interval with $T = 300 \text{ ms}$. The line color indicates unsuccessful (blue) or successful (red) defibrillation.

that succeed in defibrillation, with the energy gradually decreasing and the likelihood of unsuccessful defibrillation vanishing. (Since a decrease in \mathcal{L} does not guarantee a decrease in \mathcal{M} , there is a small likelihood that a decrease in the energy \mathcal{N} may lead to an increase in \mathcal{M} which corresponds to unsuccessful defibrillation over a narrow range of the optimization parameter s , as illustrated in Fig. 6.) The initial and final electric field profiles are compared in Fig. 7. Note that the decrease in the energy is mostly due to the decrease in the strength of the electric field over the interval corresponding to the single biphasic pulse.

Defibrillating protocols of substantially lower energy can be found using an initial condition with zero energy, i.e., $E_0(t) = 0$. We have investigated single-shot adjoint optimization for T varying from 200 to 600 ms in increments of 20 ms. In every case, the energy \mathcal{N} initially increased (with a concomitant decrease in \mathcal{L}). However, a defibrillating protocol was only obtained for $T = 200, 380$, and 400 ms , with the smallest energy achieved for the shortest T considered, illustrating the very rugged shape of the cost functional in the space of continuous functions $E(t)$. The energy can be reduced

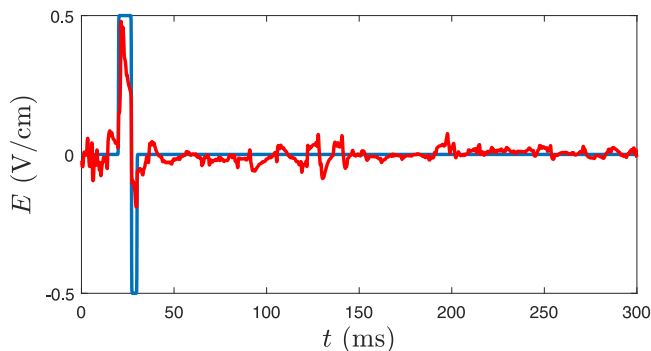


FIG. 7. Nondefibrillating single pulse (blue) and defibrillating protocol of lower energy found by adjoint optimization (red).

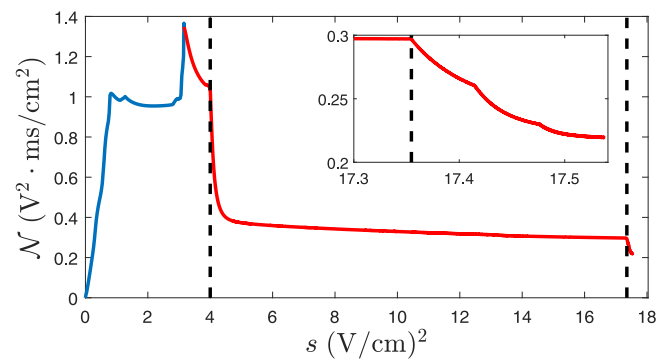


FIG. 8. (a) \mathcal{N} as a function of s for an optimization sequence with three stages of different T -values, separated by dashed lines. In the first stage, $T = 200 \text{ ms}$ and the starting electric field $E_0(t) = 0$, for $0 \leq t \leq T$. For the second and third stages, $T = 220$ and 240 ms , respectively. The red (blue) line color indicates the electric fields $E_s(t)$, which produce (do not produce) defibrillation. The inset shows the zoomed-in view of the short third stage.

further by extending the range of time over which the optimization is performed, resulting in a multi-stage procedure illustrated below.

Figure 8 shows \mathcal{N} as a function of s for an optimization procedure with three stages corresponding to $T = 200 \text{ ms}$, followed by $T = 220 \text{ ms}$ and, ultimately, $T = 240 \text{ ms}$, with the instances when T is changed marked by the vertical dashed lines. In the first stage, the energy \mathcal{N} initially increases until a successful defibrillation protocol is found at $s = 3.2 \text{ (V/cm)}^2$. The energy then starts to decrease without an increase in \mathcal{M} , so, in this case, all subsequently found electric field profiles lead to defibrillation. After a fast decrement, \mathcal{N} stagnates around $s = 4 \text{ (V/cm)}^2$. To attain a further reduction of \mathcal{N} , T is increased from 200 to 220 ms. After a quick drop, the energy starts to decrease quite slowly, prompting a further increase in T to 240 ms at $s = 17.35 \text{ (V/cm)}^2$. This allowed the energy to be reduced even further, with \mathcal{N} eventually stagnating at the value of around $0.22 \text{ V}^2 \text{ ms/cm}^2$, an improvement of more than an order of magnitude compared with the energy of the single-pulse protocol. Note that, in the third stage, the step size had to be reduced by almost two orders of magnitude compared to the second stage, so the number of iterations, and hence the computational cost, of the latter two stages is comparable. The values of the hyperparameters for the three stages are as follows: $\Delta s = \{10^{-4}, 5 \times 10^{-5}, 10^{-6}\} \text{ (V/cm)}^2$ and $\alpha = \{1, 5, 40\} \text{ cm}^2/(\text{V}^2 \text{ ms})$. For each stage, $(\gamma_1, \gamma_2, \gamma_3) = (1, 0.2, 0.2)$.

The electric field profile at the end of the first stage [$s = 4 \text{ (V/cm)}^2$] and the electric field at the end of the third stage [$s = 17.54 \text{ (V/cm)}^2$] are shown in Fig. 9(a). Both are defibrillating protocols, which lead to termination of the electrical activity at $t = 320 \text{ ms}$. Two features of the latter electric field profile are worth pointing out. First, similar to biphasic defibrillation protocols, it features a pronounced positive “pulse” at $t \approx 70 \text{ ms}$, immediately followed by a smaller negative “pulse” as shown in Fig. 9(b). Second, the electric field essentially vanishes after $t \approx 130 \text{ ms}$ (i.e., roughly one-half of the period, P), far sooner than the end of the optimization interval $T = 240 \text{ ms}$. Hence, successful defibrillation can be achieved using low energy and very quickly.

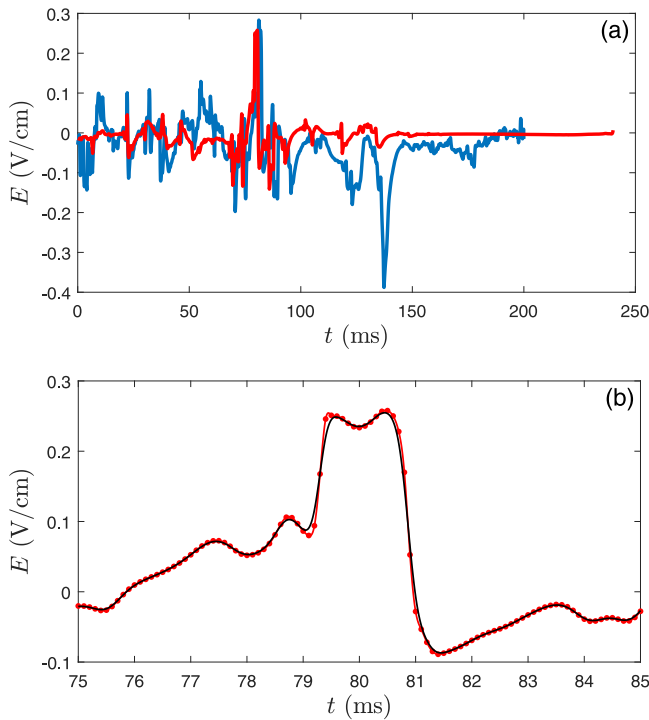


FIG. 9. (a) Electric fields found by the gradient descent sequence presented in Fig. 8, at $s = 4 \text{ (V/cm)}^2$ (blue) and $s = 17.54 \text{ (V/cm)}^2$ (red). (b) The portion of the red signal in panel (a) corresponding to the large spoke. The dots represent the value of $E(t)$ at $t_l = l\Delta t$, l integer, and the solid line is the cubic spline used to interpolate the value of $E(t)$ at each Runge-Kutta step. A slightly smoothed signal $E'(t)$ (with $\sigma = 0.1 \text{ ms}$) is shown in black.

C. Improved gradient descent

The speed of convergence of the gradient descent iteration (13) can be increased significantly using the Nesterov accelerated gradient (NAG) method.^{34,35} In this work, we used the following implementation of NAG

$$F_{s+\Delta s}(t) = E_s(t) - \Delta s \mathcal{G}(t)|_{E_s(t)}, \quad (18)$$

$$E_{s+\Delta s}(t) = F_{s+\Delta s}(t) + \beta(F_{s+\Delta s}(t) - F_s(t)),$$

where $F_0(t) = E_0(t)$ and $0 \leq \beta \leq 1$ is a tunable parameter. In particular, $\beta = 0$ corresponds to the standard gradient descent algorithm. Smaller values of β lead to a slower rate of change of $E_s(t)$, making the method more stable. Here, we illustrate NAG by identifying a defibrillating protocol on a long temporal interval with $T = 600 \text{ ms}$, where standard gradient descent fails. As we will see below, an increase in T allows further substantial reduction in energy.

We again start with $E_0(0) = 0$ for $0 \leq t \leq T$ and apply the standard gradient descent algorithm [with $\alpha = 1 \text{ cm}^2/(\text{V}^2 \text{ ms})$, $(\gamma_1, \gamma_2, \gamma_3) = (1, 0.2, 0.2)$, and $\Delta s = 10^{-6} \text{ (V/cm)}^2$], which finds electric field profiles with increasing energy that fail to achieve defibrillation, as shown in Fig. 10. At $s = 0.095 \text{ (V/cm)}^2$, we switched to

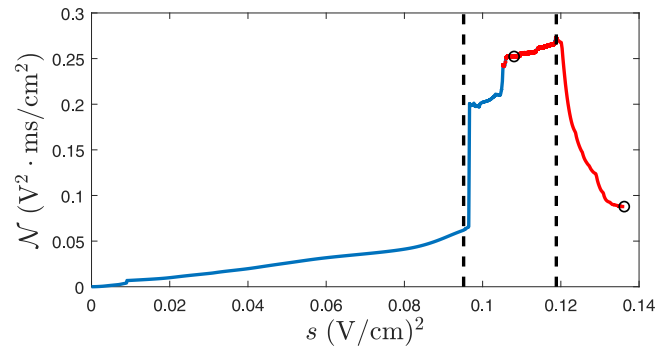


FIG. 10. \mathcal{N} as a function of s for an optimization sequence with three stages, separated by dashed lines. In the first stage, the optimization was performed by gradient descent with $T = 600 \text{ ms}$ and $E_0(t) = 0$, $0 \leq t \leq T$. In the second stage, NAG was used with T kept at 600 ms . The final stage continued to use NAG, but T was extended to 820 ms . The red (blue) line color indicates the electric fields $E_s(t)$ which produce (do not produce) defibrillation. The circles mark the s -values corresponding to the electric fields $E(t)$ shown in Fig. 11.

NAG with $\beta = 0.5$, which quickly identified a family of defibrillating protocols (corresponding to $s \geq 0.108 \text{ (V/cm)}^2$). Note that by simply continuing with the standard gradient descent, no defibrillating electric field was identified up to $s = 0.12 \text{ (V/cm)}^2$. Hence, NAG was essential for finding a defibrillating protocol.

The electric field profile corresponding to $s = 0.108 \text{ (V/cm)}^2$ is shown in Fig. 11 (blue line); its energy is $\mathcal{N} = 0.24 \text{ V}^2 \text{ ms/cm}^2$, comparable to that of the best protocol shown in Fig. 9. Further optimization using NAG with the same hyperparameters leads to a decrease in \mathcal{M} at the cost of a slightly increasing \mathcal{N} , so we chose to extend T from 600 to 820 ms at $s = 0.119 \text{ (V/cm)}^2$. This resulted in a fast decrease of \mathcal{N} , as shown in Fig. 10. The final electric field profile (red line in Fig. 11) has energy $\mathcal{N} = 0.088 \text{ V}^2 \text{ ms/cm}^2$, which corresponds to 3% of the single-pulse energy \mathcal{N}_1 and 0.1% of the characteristic LEAP energy \mathcal{N}_5 .

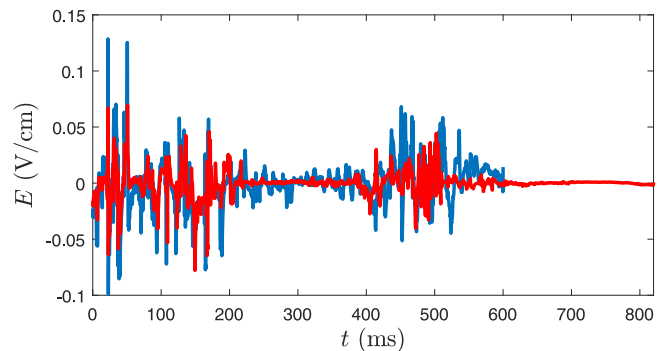


FIG. 11. Electric fields $E(t)$ corresponding to $s = 0.108 \text{ (V/cm)}^2$ (blue) and $s = 0.136 \text{ (V/cm)}^2$ (red) in Fig. 10. The corresponding values of s are indicated by circles in Fig. 10.

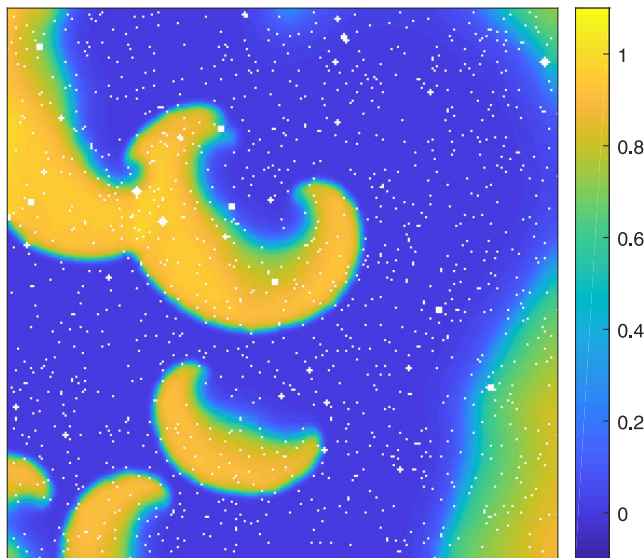


FIG. 12. Voltage field of the state with seven phase singularities corresponding to $t = 10.77$ s in the solution shown in Fig. 1, used as an initial condition for successful defibrillation. Multimedia available online.

It is worth pointing out that while NAG can substantially increase the rate of convergence, it requires a careful choice of hyperparameters β and Δs to ensure stability. For instance, NAG iterations starting with the electric field corresponding to $s = 0.095$ (V/cm)² in Fig. 10 and $\beta = 0.9$ lead to such an unstable behavior. It remains to be explored whether there are adaptive implementations of NAG with variable β and Δs that are both faster than standard gradient descent and stable.

To illustrate that the results presented above are not an artifact of a lucky choice of initial condition, in the conclusion of this section, we present an example of successful defibrillation for an initial state with a more complicated excitation pattern featuring

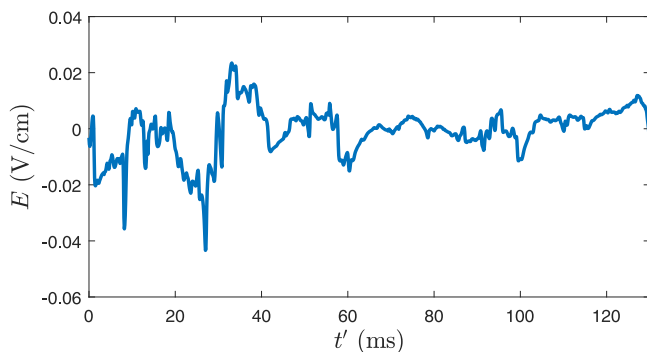


FIG. 13. Defibrillating signal $E(t)$ found for the initial condition displayed in Fig. 12 with $t' = t - 10.77$ s.

seven phases singularities. This state is shown in Fig. 12 and corresponds to $t = 10.77$ s in the time series shown in Fig. 1. NAG was used to find a low-energy defibrillating signal for this initial condition, with the interval length set to $T = 130$ ms. The defibrillating signal $E(t)$ found using $\Delta s = 10^{-4}$ (V/cm)², $\alpha = 50$ cm²/(V² ms), $\beta = 0.9$, and $(\gamma_1, \gamma_2, \gamma_3) = (1, 0.2, 0.2)$ is shown in Fig. 13. Its energy $\mathcal{N} = 0.010$ V² ms/cm² is lower than the smallest energy of the protocols found for the initial condition with two phase singularities. This energy corresponds to just 0.01% of the characteristic LEAP energy \mathcal{N}_5 .

IV. DISCUSSION AND CONCLUSIONS

In this study, a simple two-dimensional numerical model of atrial tissue containing anatomical heterogeneities—the essential ingredient responsible for the emergence of virtual electrodes—was used to explore ultra-low-energy defibrillation. The approach considered here is impractical—it requires an accurate mathematical model of the tissue as well as complete knowledge of the state of the tissue at the initial time. Furthermore, computation of a defibrillating electrical field cannot be performed in real time. However, our results provide a number of important lessons.

Despite the state of fibrillation—in the model and for the parameters considered here—persisting over a very long temporal interval, fibrillation appears to be a long chaotic transient rather than a sustained state. This implies that fibrillation will eventually disappear on its own, so the lowest defibrillation energy approaches zero as the interval length T is increased, as noted previously by Lilienskamp and Parlitz.³⁶ Indeed, we found that, using adjoint optimization, the energy required for defibrillation can be reduced by three(!) orders of magnitude compared with current state-of-the-art protocols such as LEAP. There is little doubt that this energy could be reduced even further by using better initial conditions, improved gradient descent algorithms, or additional tuning of the hyperparameters (e.g., the choice of the weights α and γ_i used in defining the cost function).

All of the defibrillating signals identified via adjoint optimization feature high-frequency oscillation with time scale of order 10 ms. Note that this time scale is essentially identical to the duration of an optimal biphasic pulse.²² This time scale is also comparable to that describing the dynamics of the fast gating variable (u_2), which controls the repolarization dynamics and conduction velocity. In contrast, the slow gating variable (u_3) which controls the action potential duration, evolves on a much longer time scale. Hence, the applied electric field largely plays the role of the fast gating variable in modulating the slow outward current. These fast oscillations appear to be an essential property of defibrillating protocols rather than an artifact of adjoint optimization: applying even a minor amount of smoothing,

$$E'(t) = \frac{1}{\sqrt{\pi}\sigma} \int_{-\infty}^{\infty} e^{-(t-t')^2/\sigma^2} E(t') dt', \quad (19)$$

to the computed electric field, with σ of order 0.1 ms, leads to a failure of defibrillation.

Given that the maximal strength of the electric field is quite small, it is clear that virtual electrodes do not generate new wavefronts and phase singularities. Rather, the effect of the electric field

is to gently alter the motion of existing phase singularities. Since phase singularities cannot be created or destroyed by weak electric fields, defibrillation can be achieved by one or both of the following mechanisms: (i) individual phase singularities, regardless of their topological charge, can be swept across the boundary, i.e., outside of the tissue, or (ii) pairs of phase singularities with opposite topological charges can be mutually annihilated inside the tissue. While drift and interaction of spiral waves induced by near-resonant time-periodic electric fields are well-understood,^{11,12} the impact of aperiodic high-frequency electric fields has received little attention so far.

This study provides the first insight into how weak aperiodic electric fields can affect the dynamics. For the initial condition with two phase singularities, the movies illustrating the evolution of the excitation waves with the defibrillating electric field $E(t)$ shown in red in Fig. 9, with its slightly smoothed version $E'(t)$, as well without an applied electric field are included as multimedia files (available online). These movies also show the dynamics of the associated phase singularities computed using the level-set-based approach.³⁷ These movies clearly demonstrate that defibrillation is achieved through mechanism (ii). Figure 14 shows the snapshots of the state for the three cases about 30 ms after a short wavefront (connecting a pair of nearby phase singularities with opposite topological charge, shown as white/black circles) passes through a region of nearly refractory tissue behind the trailing edge of another excitation wave.

This region is characterized by low conduction velocity and low excitability, so any wave passing through it is extremely susceptible to very small perturbations. Such vulnerable windows³⁸ have been a target of defibrillation protocols for a long time.^{39–41} Without an applied electric field, the excitation wave manages to pass through with the two phase singularities never approaching each other too closely. The defibrillating signal $E(t)$ delays repolarization, slowing

down the excitation wave sufficiently to produce conduction block and annihilation of the two phase singularities. The smoothed signal $E'(t)$ brings the two phase singularities closer to each other but not enough to lead to their annihilation. The conditions under which phase singularities merge and an excitation wave collapses were discussed in Ref. 42. Note that this mechanism differs from that identified by Buran *et al.*³¹ for LEAP, which aims to minimize the likelihood of creating new phase singularities.

The same mechanism is also found to be at play during successful defibrillation of the initial state with seven phase singularities shown in Fig. 12, as illustrated by the corresponding multimedia available online. In this case, there is a succession of events where pairs of phase singularities with opposite topological charges are mutually annihilated as they pass through vulnerable windows. Low-energy defibrillation protocols can exploit many such windows that open up naturally at different times and in different regions, as the excitation pattern evolves.

The possibility of leveraging this defibrillation mechanism raises an interesting question regarding the statement of the optimization problem. Fibrillation can be terminated by decreasing spatial gradients of the voltage and the gating variables, as shown here, but the same result can also be achieved by eliminating phase singularities. The latter objective can be targeted directly by a suitable modification of the cost function. For instance, a positive-definite function $\mathcal{M} = |\nabla u_i \times \nabla u_j|^2$ with $i \neq j$ will be strongly peaked at the cores of the spiral waves surrounding phase singularities. Minimization of a respective cost function should produce electric fields that lead to pair-wise elimination of counter-rotating spiral waves. This can produce even more efficient defibrillation protocols and is worth being explored further.

Let us conclude by a discussion of which of our specific results would generalize and which would not. Indeed, this study was limited to a particular ionic model with a specific choice of parameters

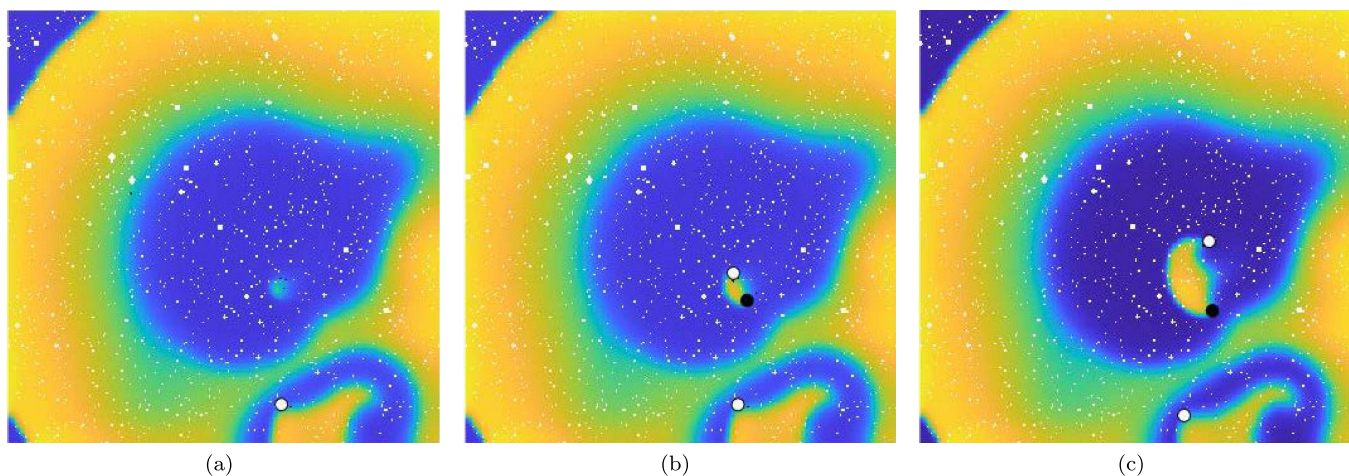


FIG. 14. Snapshots of the voltage field (u_i) at $t = 174$ ms for three different choices of the applied electric field: (a) electric field profile $E(t)$ shown in red in Fig. 9, (b) its smoothed version $E'(t)$ with $\sigma = 0.1$ ms, and (c) no electric field, i.e., $E(t) = 0$. The white and black circles mark the phase singularities with positive (negative) topological charge. The same colorbar as in Fig. 1 is used. The remaining phase singularity at the bottom of the panels will leave the domain by $t = 203$ ms in every case. Multimedia available online.

and distribution of heterogeneities. A particular defibrillating protocol that works for one such choice almost certainly would not work for another. In fact, even a slightly different initialization of $E(t)$ can lead to a dramatically different defibrillation protocol. This is a consequence of the cost function “landscape” of this problem being very rough, with lots of local minima. The statistics of these landscapes, on the other hand, are likely quite robust, with many local minima associated with energies close to the global minimum energy \mathcal{N} , which vanishes with increasing T . Hence, one will generally be able to find *some* defibrillating protocol with an arbitrarily low energy, provided T is chosen large enough. All such protocols would likely exploit the same physical mechanism identified here.

ACKNOWLEDGMENTS

We would like to thank Christopher Marcotte for bringing to our attention a WebGL solver for the Fenton–Karma model,⁴³ which was used for exploring the behavior of solutions for different parameter sets. We would also like to thank Daniel Gurevich for help with the topological analysis of the data.

AUTHOR DECLARATIONS

Conflict of Interest

The authors have no conflicts to disclose.

Author Contributions

Alejandro Garzon: Conceptualization (equal); Investigation (lead); Methodology (lead); Software (lead); Visualization (lead); Writing – original draft (lead); Writing – review & editing (equal). **Roman O. Grigoriev:** Conceptualization (equal); Formal analysis (lead); Methodology (supporting); Resources (lead); Visualization (supporting); Writing – original draft (supporting); Writing – review & editing (equal).

DATA AVAILABILITY

The data that support the findings of this study are available from the corresponding author upon reasonable request.

APPENDIX A: COMPUTATION OF THE FUNCTIONAL DERIVATIVE

Note that the cost function \mathcal{L} depends on $E(t)$ both explicitly through $\mathcal{N}[E]$ and implicitly through $\mathcal{M}[\mathbf{u}]$, so its functional derivative $\mathcal{G} = \delta\mathcal{L}/\delta E$ cannot be written in an explicit analytical form as is often the case in variational calculus. Instead, we can compute it using the formal definition⁴⁴

$$\langle \mathcal{G}, \phi \rangle = \left(\frac{d}{d\varepsilon} \mathcal{L}[E(t) + \varepsilon\phi(t)] \right)_{\varepsilon=0}, \quad (\text{A1})$$

where $\phi(t)$ is an arbitrary function and, in this section, the angle brackets denote the Euclidean inner product

$$\langle f, g \rangle = \int_0^T f(t)g(t) dt. \quad (\text{A2})$$

For a numerical solution evaluated at a discrete set of time steps $t_l = l\Delta t$ with $l = 0, \dots, N$, we can evaluate the function derivative by using $\phi_l(t) = \delta(t - t_l)$, where $\delta(t)$ is the Dirac delta function, such that

$$\langle \mathcal{G}, \phi_l \rangle = \int_0^T \mathcal{G}(t) \delta(t - t_l) dt = \mathcal{G}(t_l).$$

Evaluating the derivative in the definition (A1) using finite differences, we find

$$\mathcal{G}(t_l) \approx \frac{\mathcal{L}[E(t) + \varepsilon\delta(t - t_l)] - \mathcal{L}[E(t)]}{\varepsilon} \quad (\text{A3})$$

for a sufficiently small ε . Note that in order to evaluate the functional derivative using (A3) at any one time step, the solution $\mathbf{u}(t, \mathbf{r})$ should be evaluated at all N time steps. Hence, the total number of operations involved in evaluating $\mathcal{G}(t)$ on the interval $t \in [0, T]$ scales as $N(N+1) \sim N^2$.

APPENDIX B: SPATIAL DISCRETIZATION

For the purpose of spatial discretization, the circular conduction heterogeneities were approximated by polygons with sides parallel to either the x or y axis. The corresponding normal vector \mathbf{n} is, therefore, equal to $\pm\hat{\mathbf{y}}$ or $\pm\hat{\mathbf{x}}$, respectively.

For interior points, the Laplacian $\nabla^2 u_i$ was approximated using the second-order centered finite differences formula

$$\nabla^2 u_i(\mathbf{r}_j) \approx \frac{u_{ijL} + u_{iT} - 4u_{ij} + u_{ijB} + u_{ijR}}{(\Delta x)^2}, \quad (\text{B1})$$

where j_L, j_T, j_B , and j_R are, respectively, the indices of the left, top, bottom, and right neighbor of the j th grid point. For points on the boundary, the missing neighbor(s) are replaced by fictitious ones and the boundary conditions (2) and (3) are used to compute the value of u_i at those ghost points.⁴⁵ For instance, if the point j is on a boundary segment with $\mathbf{n} = \hat{\mathbf{x}}$, its right neighbor is a ghost point. Assuming no other neighbor is missing, the Laplacian $\nabla^2 u_1$ is approximated by the analog of Eq. (B1),

$$\nabla^2 u_1(\mathbf{r}_j) \approx \frac{u_{1jL} + u_{1jT} - 4u_{1j} + u_{1jB} + u_1^G}{(\Delta x)^2}, \quad (\text{B2})$$

where u_1^G is the value of u_1 at the ghost right neighbor. To compute u_1^G , notice that, when $\mathbf{n} = \hat{\mathbf{x}}$, the boundary condition (2) reduces to

$$\frac{\partial u_1}{\partial x} - E = 0. \quad (\text{B3})$$

Approximating the derivative in (B3) with the second-order centered finite differences formula, we get

$$\frac{u_1^G - u_{1jL}}{2\Delta x} - E \approx 0. \quad (\text{B4})$$

Solving for u_1^G in (B4) and substituting the result into (B2), we have

$$D_1 \nabla^2 u_1(\mathbf{r}_j) \approx \sigma (2u_{1jL} + u_{1jT} - 4u_{1j} + u_{1jB}) + \mu E, \quad (\text{B5})$$

where

$$\sigma = \frac{D_1}{(\Delta x)^2} \text{ and } \mu = \frac{2D_1}{\Delta x}. \quad (\text{B6})$$

Grid points missing other neighbors are dealt with analogously. The discretization of $\nabla^2 u_i$, $i \geq 2$, for boundary points, where (3) holds,

produces expressions similar to (B5) but without the term involving the electric field. Consequently, the discretization of the term $\tilde{\mathbf{L}}\mathbf{u}$ in Eq. (1) can be written in the form

$$\mathbf{L}\mathbf{w} + \mathbf{E}\mathbf{b}, \quad (\text{B7})$$

where \mathbf{L} is an $mn \times mn$ block-diagonal matrix (with diagonal blocks of size $m \times m$) and \mathbf{b} is a column vector with mn elements. Hence, the evolution equation takes the form

$$\dot{\mathbf{w}} \approx \mathbf{L}\mathbf{w} + \mathbf{F}(\mathbf{w}) + \mathbf{E}\mathbf{b}, \quad (\text{B8})$$

where the column vector \mathbf{F} describes the ionic model.

One can similarly write the functionals \mathcal{J}_i in terms of the discretized state vector. Let $\mathbf{w}_i = [u_{i,1}, u_{i,2}, \dots, u_{i,m}]^T$ such that $\mathbf{w} = [\mathbf{w}_1^T, \mathbf{w}_2^T, \dots, \mathbf{w}_n^T]^T$. Furthermore, let us denote the values of the spatial derivatives $\partial_x u_i$ and $\partial_y u_i$ on the computational grid, respectively, as $G_x \mathbf{w}_i$ and $G_y \mathbf{w}_i$, where G_x and G_y are $m \times m$ matrices representing the second-order finite differences approximations of the derivatives. With the help of this notation, we can write

$$\mathcal{J}_i \approx [\mathbf{w}_i^T \mathbf{S} \mathbf{w}_i]_{t=T},$$

where $\mathbf{S} = [G_x^T G_x + G_y^T G_y](\Delta x)^2$, and

$$\mathcal{L} \approx \frac{1}{2} [\mathbf{w}^T \mathbf{R} \mathbf{w}]_{t=T} + \frac{\alpha}{2} \int_0^T E^2 dt, \quad (\text{B9})$$

where \mathbf{R} is an $nm \times nm$ block-diagonal matrix with the i th $m \times m$ diagonal block equal to $\gamma_i \mathbf{S}$, $i = 1, 2, \dots, n$.

APPENDIX C: DERIVATION OF THE ADJOINT EQUATIONS

In this section, we consider a minimization problem for the functional (B9) subject to the dynamical constraint (B8) for all $t \in [0, T]$, which we will rewrite as

$$\mathbf{q}[E, \mathbf{w}] = \dot{\mathbf{w}} - \mathbf{L}\mathbf{w} - \mathbf{F}(\mathbf{w}) - \mathbf{E}\mathbf{b} = \mathbf{0}. \quad (\text{C1})$$

By introducing a Lagrange multiplier $\lambda(t)$, it can be converted to an unconstrained minimization problem for the new functional

$$\mathcal{L}'[E, \mathbf{w}, \lambda] = \mathcal{L} - \langle \lambda, \mathbf{q} \rangle, \quad (\text{C2})$$

where, in this section, the angle brackets denote the inner product

$$\langle \mathbf{f}, \mathbf{g} \rangle = \int_0^T [\mathbf{f}(t)]^T \mathbf{g}(t) dt. \quad (\text{C3})$$

Note that, for \mathbf{w} which satisfies the governing equations, $\mathbf{q} = \mathbf{0}$, so $\mathcal{L}' = \mathcal{L}$. Applying the chain rule, we find

$$\frac{\delta \mathcal{L}}{\delta E(t)} = \frac{\partial \mathcal{L}'}{\partial E(t)} + \int_0^T \frac{\partial \mathcal{L}'}{\partial \mathbf{w}(s)} \frac{\delta \mathbf{w}(s)}{\delta E(t)} ds + \int_0^T \frac{\partial \mathcal{L}'}{\partial \lambda(s)} \frac{\delta \lambda(s)}{\delta E(t)} ds, \quad (\text{C4})$$

where the last term on the right-hand side vanishes, since

$$\frac{\partial \mathcal{L}'}{\partial \lambda} = \mathbf{q} = \mathbf{0}. \quad (\text{C5})$$

The second term can also be eliminated by requiring

$$\frac{\partial \mathcal{L}'}{\partial \mathbf{w}} = \mathbf{0}. \quad (\text{C6})$$

Holding variables \mathbf{w} and λ , the functional derivative can now be evaluated using the definition (A1),

$$\mathcal{G} = \frac{\delta \mathcal{L}}{\delta E} = \frac{\partial \mathcal{L}'}{\partial E} = \alpha E + \lambda^T \mathbf{b}, \quad (\text{C7})$$

which requires the knowledge of $\lambda(t)$ on the interval $t \in [0, T]$. The governing equations for the Lagrange multiplier can be derived using the condition (C6),

$$\frac{1}{2} \frac{\partial}{\partial \mathbf{w}} [\mathbf{w}^T \mathbf{R} \mathbf{w}]_{t=T} - \frac{\partial}{\partial \mathbf{w}} \langle \lambda, \dot{\mathbf{w}} \rangle + \frac{\partial}{\partial \mathbf{w}} \langle \lambda, \mathbf{L}\mathbf{w} + \mathbf{F}(\mathbf{w}) \rangle = \mathbf{0}, \quad (\text{C8})$$

where the temporal derivative can be moved from \mathbf{w} to λ via integration by parts,

$$\langle \lambda, \dot{\mathbf{w}} \rangle = \lambda^T(T) \mathbf{w}(T) - \lambda^T(0) \mathbf{w}(0) - \langle \dot{\lambda}, \mathbf{w} \rangle. \quad (\text{C9})$$

It is straightforward to show that

$$\frac{\partial}{\partial \mathbf{w}(T)} [\mathbf{w}^T \mathbf{R} \mathbf{w}]_{t=T} = 2 \mathbf{R} \mathbf{w}(T), \quad (\text{C10a})$$

$$\frac{\partial}{\partial \mathbf{w}(T)} [\lambda^T(T) \mathbf{w}(T)] = \lambda(T), \quad (\text{C10b})$$

$$\frac{\partial}{\partial \mathbf{w}(0)} [\lambda^T(0) \mathbf{w}(0)] = \mathbf{0}, \quad (\text{C10c})$$

$$\frac{\partial}{\partial \mathbf{w}(t)} \langle \dot{\lambda}(t), \mathbf{w}(t) \rangle = \dot{\lambda}(t), \quad (\text{C10d})$$

$$\frac{\partial}{\partial \mathbf{w}(t)} \langle \lambda(t), \mathbf{L}\mathbf{w}(t) + \mathbf{F}(\mathbf{w}(t)) \rangle = \mathbf{L}^T \lambda(t) + \mathbf{J}_F^T \lambda(t), \quad (\text{C10e})$$

where Eq. (C10c) is a consequence of the fixed initial condition $\mathbf{w}(0) = \mathbf{w}_0$. Evaluating the partial derivatives in Eq. (C8) at $t = T$ yields the initial condition (11b), while evaluating the partial derivatives for $0 < t < T$ yields the evolution Eq. (11a).

Let us conclude this section by estimating the number of operations required to evaluate the functional derivative \mathcal{G} using the adjoint method. Integration of the evolution Eq. (9a) to compute $\mathbf{w}(t)$ on the interval $[0, T]$ requires $O(N)$ operations. Integration of Eq. (11a) to compute $\lambda(t)$ on the interval $[0, T]$ also requires $O(N)$ operations, although, in the latter case, one time step is more costly than in the former case due to the larger number of arithmetic and memory transfer operations required to calculate the n^2 elements of the Jacobian \mathbf{J}_F compared with just n elements of \mathbf{F} . Nonetheless, since the total number of operations scales linearly with N , the adjoint method is substantially less expensive than the finite differences method described in Appendix A, which requires a number of operations that scales as N^2 .

APPENDIX D: COMPUTATION OF THE SPECTRAL DENSITY

The spectral density $W(f)$ is computed in the following manner. The Fast Fourier Transform $U(f_l, \mathbf{r}_i)$ of $u_1(t_l, \mathbf{r}_i)$, where $t_l = l\Delta t$, $l = 1, 2, \dots, N$, $N = 2.5 \times 10^5$, and the frequencies $f_l = l/(N\Delta t)$, was computed for a hundred evenly spaced locations \mathbf{r}_i . Then, the

local power spectral density $W(f, \mathbf{r}_i)$ (subscript l dropped) was calculated as $|U(f, \mathbf{r}_i)|^2$ normalized by the mean squared amplitude of $u_l(t, \mathbf{r}_i)$.⁴⁶ Finally, the global power spectral density $W(f)$, shown in Fig. 2, was determined as the average of the $W(f, \mathbf{r}_i)$ over all the sampled locations \mathbf{r}_i .

REFERENCES

- ¹C. X. Wong, A. Brown, D. H. Lau, S. S. Chugh, C. M. Albert, J. M. Kalman, and P. Sanders, "Epidemiology of sudden cardiac death: Global and regional perspectives," *Heart, Lung Circ.* **28**, 6–14 (2019).
- ²C. W. Tsao, A. W. Aday, Z. I. Almarzooq, A. Alonso, A. Z. Beaton, M. S. Bittencourt, A. K. Boehme, A. E. Buxton, A. P. Carson, Y. Comodore-Mensah *et al.*, "Heart disease and stroke statistics—2022 update: A report from the American Heart Association," *Circulation* **145**, e153–e639 (2022).
- ³T. M. Munger, L.-Q. Wu, and W. K. Shen, "Atrial fibrillation," *J. Biomed. Res.* **28**, 1–17 (2014).
- ⁴S. S. Chugh, R. Havmoeller, K. Narayanan, D. Singh, M. Rienstra, E. J. Benjamin, R. F. Gillum, Y.-H. Kim, J. H. McNulty Jr, Z.-J. Zheng *et al.*, "Worldwide epidemiology of atrial fibrillation: A global burden of disease 2010 study," *Circulation* **129**, 837–847 (2014).
- ⁵R. Passman and A. Kadish, "Shouldn't everyone have an implantable cardioverter-defibrillator?," *Circulation* **120**(22), 2166–2167 (2009).
- ⁶C. F. Babbs, W. A. Tacker, J. F. VanVleet, J. D. Bourland, and L. A. Geddes, "Therapeutic indices for transchest defibrillator shocks: Effective, damaging, and lethal electrical doses," *Am. Heart J.* **99**, 734–738 (1980).
- ⁷A. E. Epstein, P. G. Anderson, G. N. Kay, S. M. Dailey, V. J. Plumb, and R. B. Shepard, "Gross and microscopic changes associated with a nonthoracotomy implantable cardioverter defibrillator," *Pacing Clin. Electrophysiol.* **15**, 382–386 (1992).
- ⁸S. F. Sears, J. D. Hauf, K. Kirian, G. Hazelton, and J. B. Conti, "Posttraumatic stress and the implantable cardioverter-defibrillator patient: What the electrophysiologist needs to know," *Circ.: Arrhythmia Electrophysiol.* **4**, 242–250 (2011).
- ⁹F. Jacq, G. Foulldrin, A. Savouré, F. Anselme, A. Baguelin-Pinaud, A. Cribier, and F. Thibaut, "A comparison of anxiety, depression and quality of life between device shock and nonshock groups in implantable cardioverter defibrillator recipients," *Gen. Hosp. Psychiatry* **31**, 266–273 (2009).
- ¹⁰K. I. Agladze, V. A. Davydov, and A. S. Mikhailov, "Observation of a helical-wave resonance in an excitable distributed medium," *JETP Lett.* **45**, 767–770 (1987).
- ¹¹V. Biktashev and A. Holden, "Design principles of a low voltage cardiac defibrillator based on the effect of feedback resonant drift," *J. Theor. Biol.* **169**, 101–112 (1994).
- ¹²V. Biktashev and A. Holden, "Resonant drift of autowave vortices in two dimensions and the effects of boundaries and inhomogeneities," *Chaos, Solitons Fractals* **5**, 575–622 (1995).
- ¹³S. Luther, F. H. Fenton, B. G. Kornreich, A. Squires, P. Bittihn, D. Hornung, M. Zabel, J. Flanders, A. Gladuli, L. Campoy, E. M. Cherry, G. Luther, G. Hasenfuss, V. I. Krinsky, A. Pumir, R. F. Gilmour, and E. Bodenschatz, "Low-energy control of electrical turbulence in the heart," *Nature* **475**, 235–239 (2011).
- ¹⁴P. Buran, M. Bär, S. Alonso, and T. Niedermayer, "Control of electrical turbulence by periodic excitation of cardiac tissue," *Chaos* **27**, 113110 (2017).
- ¹⁵Y. C. Ji, I. Uzelac, N. Otani, S. Luther, R. F. Gilmour Jr, E. M. Cherry, and F. H. Fenton, "Synchronization as a mechanism for low-energy anti-fibrillation pacing," *Heart Rhythm* **14**, 1254–1262 (2017).
- ¹⁶T. Lilienskamp, U. Parlitz, and S. Luther, "Taming cardiac arrhythmias: Terminating spiral wave chaos by adaptive deceleration pacing," *Chaos* **32**, 121105 (2022).
- ¹⁷D. Wilson and J. Moehlis, "Toward a more efficient implementation of antifibrillation pacing," *PLoS One* **11**, e0158239 (2016).
- ¹⁸F. S. Ng, O. Toman, J. Petru, P. Peichl, R. A. Winkle, V. Y. Reddy, P. Neuzil, R. H. Mead, N. A. Qureshi, Z. I. Whinnett *et al.*, "Novel low-voltage multi-pulse therapy to terminate atrial fibrillation," *Clin. Electrophysiol.* **7**, 988–999 (2021).
- ¹⁹N. DeTal, A. Kaboudian, and F. H. Fenton, "Terminating spiral waves with a single designed stimulus: Teleportation as the mechanism for defibrillation," *Proc. Natl. Acad. Sci.* **119**, e2117568119 (2022).
- ²⁰M. R. Gold, N. Sulke, D. S. Schwartzman, R. Mehra, and D. E. Euler, "Clinical experience with a dual-chamber implantable cardioverter defibrillator to treat atrial tachyarrhythmias," *J. Cardiovasc. Electrophysiol.* **12**, 1247–1253 (2001).
- ²¹F. M. Merchant, T. Quest, A. R. Leon, and M. F. El-Chami, "Implantable cardioverter-defibrillators at end of battery life: Opportunities for risk (re)-stratification in ICD recipients," *J. Am. Coll. Cardiol.* **67**, 435–444 (2016).
- ²²J. Bragard, A. Simic, J. Elorza, R. O. Grigoriev, E. M. Cherry, R. F. Gilmour, N. F. Otani, and F. H. Fenton, "Shock-induced termination of reentrant cardiac arrhythmias: Comparing monophasic and biphasic shock protocols," *Chaos* **23**, 043119 (2013).
- ²³N. Chamakuri, K. Kunisch, and G. Plank, "Application of optimal control to the cardiac defibrillation problem using a physiological model of cellular dynamics," *Appl. Numer. Math.* **95**, 130–139 (2015).
- ²⁴M. Aron, T. Lilienskamp, S. Luther, and U. Parlitz, "Optimising low-energy defibrillation in 2D cardiac tissue with a genetic algorithm," *Front. Netw. Physiol.* **3**, 1172454 (2023).
- ²⁵A. Pumir and V. Krinsky, "Unpinning of a rotating wave in cardiac muscle by an electric field," *J. Theor. Biol.* **199**, 311–319 (1999).
- ²⁶R.-E. Plessix, "A review of the adjoint-state method for computing the gradient of a functional with geophysical applications," *Geophys. J. Int.* **167**, 495–503 (2006).
- ²⁷C. C. T. Pringle and R. R. Kerswell, "Using nonlinear transient growth to construct the minimal seed for shear flow turbulence," *Phys. Rev. Lett.* **105**, 154502 (2010).
- ²⁸M. J. Krause, G. Thäter, and V. Heuveline, "Adjoint-based fluid flow control and optimisation with lattice Boltzmann methods," *Comput. Math. Appl.* **65**, 945–960 (2013).
- ²⁹R. Nies, E. J. Paul, S. R. Hudson, and A. Bhattacharjee, "Adjoint methods for quasi-symmetry of vacuum fields on a surface," *J. Plasma Phys.* **88**, 905880106 (2022).
- ³⁰F. Fenton and A. Karma, "Vortex dynamics in three-dimensional continuous myocardium with fiber rotation: Filament instability and fibrillation," *Chaos* **8**, 20–47 (1998).
- ³¹P. Buran, T. Niedermayer, and M. Bär, "Mechanism of defibrillation of cardiac tissue by periodic low-energy pacing," *bioRxiv* 2023-03 (2023).
- ³²T. M. Schneider, B. Eckhardt, and J. A. Yorke, "Turbulence transition and the edge of chaos in pipe flow," *Phys. Rev. Lett.* **99**, 034502 (2007).
- ³³J. Steyer, T. Lilienskamp, S. Luther, and U. Parlitz, "The role of pulse timing in cardiac defibrillation," *Front. Netw. Physiol.* **2**, 1007585 (2023).
- ³⁴X. Liu, W. Tao, and Z. Pan, "A convergence analysis of Nesterov's accelerated gradient method in training deep linear neural networks," *Inf. Sci.* **612**, 898–925 (2022).
- ³⁵W. Su, S. Boyd, and E. J. Candès, "A differential equation for modeling Nesterov's accelerated gradient method: Theory and insights," *J. Mach. Learn. Res.* **17**, 1–43 (2016).
- ³⁶T. Lilienskamp and U. Parlitz, "Terminating transient chaos in spatially extended systems," *Chaos* **30**, 051108 (2020).
- ³⁷D. R. Gurevich and R. O. Grigoriev, "Robust approach for rotor mapping in cardiac tissue," *Chaos* **29**, 053101 (2019).
- ³⁸C. F. Starmer, V. N. Biktashev, D. N. Romashko, M. R. Stepanov, O. N. Makarova, and V. I. Krinsky, "Vulnerability in an excitable medium: Analytical and numerical studies of initiating unidirectional propagation," *Biophys. J.* **65**, 1775–1787 (1993).
- ³⁹C. F. Starmer, "The cardiac vulnerable period and reentrant arrhythmias: Targets of anti- and proarrhythmic processes," *Pacing Clin. Electrophysiol.* **20**, 445–454 (1997).
- ⁴⁰V. Biktashev and A. Holden, "Reentrant waves and their elimination in a model of mammalian ventricular tissue," *Chaos* **8**, 48–56 (1998).
- ⁴¹Y. Yamanouchi, Y. Cheng, P. J. Tchou, and I. R. Efimov, "The mechanisms of the vulnerable window: The role of virtual electrodes and shock polarity," *Can. J. Physiol. Pharmacol.* **79**, 25–33 (2001).
- ⁴²C. D. Marcotte and R. O. Grigoriev, "Dynamical mechanism of atrial fibrillation: A topological approach," *Chaos* **27**, 093936 (2017).

⁴³The CHAOS lab at Georgia Tech, see <https://chaos.gatech.edu/NGL2.0/2D-3V-Model/> for “A WebGL solver for the Fenton-Karma model” (accessed 16 May 2024).

⁴⁴R. G. Parr and W. Yang, *Density-Functional Theory of Atoms and Molecules* (Oxford, New York, 1989).

⁴⁵J. W. Thomas, *Numerical Partial Differential Equations: Finite Difference Methods* (Springer, New York, 1995).

⁴⁶W. H. Press, S. A. Teukolsky, W. T. Vetterling, and B. P. Flannery, *Numerical Recipes in C: The Art of Scientific Computing* (Cambridge University Press, Cambridge, 1992).